photonics

MDPI

Communication

Theoretical Analysis of Continuous-Wave Mid-Infrared Optical Vortex Source Generated by Singly Resonant Optical Parametric Oscillator

Ziheng Zhou, Shirui Zhang, Yuanhao Duan, Minghao Guo and Peng Li *

School of Physics and Electronics, Henan University, Kaifeng 475004, China
* Correspondence: lilipengpeng@vip.henu.edu.cn

Abstract: Due to the important application in the study of vibrational circular dichroism and helical dichroism of chiral molecules, the tunable vortex beam at mid-infrared region has attracted increasing attention. Based on orbital angular momentum (OAM) conservation in nonlinear interactions, the vortex pumped singly resonant optical parametric oscillator (SRO) is recognized as a versatile source of coherent vortex radiation providing high power and broad wavelength coverage from a single device. However, the low parametric gain and high oscillation threshold under continuous wave (cw) pumping has so far been the most challenging factor in generating cw tunable vortex beams. To predict the output characteristic of vortex pumped SRO, a theoretical model describing the vortex pumped SRO is needed. In this study, the theoretical model describing the vortex pumped SRO is set up under collimated Gaussian beam approximation. Output characteristics of different SROs are simulated numerically. By proper selection of pump scheme (such as double-pass pumping scheme), the vortex pumped mid-infrared SRO can oscillate at a relatively low pump power. By controlling the gain (mode overlap ratio between the pump and resonant wave in the nonlinear crystal) and loss (employing a spot-defect mirror with different defect size as the output coupler) of the resonant signal mode in the SRO, the OAM of the pump beam can be directionally transferred to a specific down converted beam. The transfer mechanism of the OAM among the pump light and the down-converted beams and factors affecting the transfer are studied. Our study provides the guidelines for the design and optimization of vortex pumped SRO under cw operation.

Keywords: vortex beam; singly resonant optical parametric oscillator; single-pass pumping scheme; double-pass pumping scheme; mode overlap ratio; spot-defect mirror

check for updates

Citation: Zhou, Z.; Zhang, S.; Duan, Y.; Guo, M.; Li, P. Theoretical Analysis of Continuous-Wave Mid-Infrared Optical Vortex Source Generated by Singly Resonant Optical Parametric Oscillator. *Photonics* **2022**, *9*, 1002. https://doi.org/10.3390/photonics9121002

Received: 26 November 2022
Accepted: 16 December 2022
Published: 19 December 2022

Publisher's Note: MDPI stays neutral with regard to jurisdictional claims in published maps and institutional affiliations.

Copyright: © 2022 by the authors. Licensee MDPI, Basel, Switzerland. This article is an open access article distributed under the terms and conditions of the Creative Commons Attribution (CC BY) license (https://creativecommons.org/licenses/by/4.0/).

1. Introduction

Chirality is the most common feature in nature and widely exists in living organisms, such as amino acids, sugars, DNA, etc. Optical fields with chirality are divided into circularly polarized light fields carrying spin angular momentum (SAM) and vortex light fields carrying orbital angular momentum (OAM) [1]. The difference between the absorption of left-handed and right-handed circularly polarized light by chiral molecules is called circular dichroism (CD). Similarly, the absorption difference of a chiral object to the opposite OAM state light beam is referred to as helical dichroism (HD) or OAM dichroism [2]. The researchers analyzed the interaction between OAM and different chiral substances [3–6] and realized the recognition of chiral substances based on HD spectroscopy [7]. The interaction mechanism between SAM and chiral substances has been proved in the dipole. However, in the dipole approximation, whether the light with OAM interacts with chiral objects has been controversial [2]. The study on the interaction between chiral substances and the OAM light field can not only deepen the understanding of the mechanism, but also provide a new vision for the detection of chiral substances. Due to the containing of the chemical bonds such as O-H/N-H/C-H, most chiral molecules exhibit strong absorption of light at 3–5 μm. It is particularly important to generate high quality tunable optical sources

containing OAM. The typical vortex beam (VB) usually contains an exp(i$l\phi$) term, and each photon of the VB carries the OAM of $l\hbar$ ($\hbar$ is the reduced Planck constant). Based on the OAM conservation in nonlinear frequency conversion, tunable vortex lasers at mid-IR range have been generated by vortex pumped optical parametric amplifiers [8] or optical parametric oscillators (OPO) [9–32]. In addition, the OAM conservation in a nonlinear process also allows the use of quantum resources (OAM sate) in quantum state generation and measurement [33–35]. Compared with other OPOs, although the threshold of the singly resonant OPO (SRO) is higher, it can achieve stable, high-power tunable output without locking the cavity length. Therefore, the vortex pumped SRO is an ideal choice for generating stable and high power tunable mid-infrared vortex lasers.

Researchers have undertaken a lot of work in the area of vortex pumped OPO. At the early stage, limited by the high oscillation threshold of continuous wave (cw) SRO, studies about vortex pumped OPO mainly focused on the doubly resonant or triply resonant OPO or pulse vortex pumped SRO. Early in 1999, Padgett MJ and coworkers presented the first vortex pumped OPO and verified the OAM conservation during the optical parametric process [9]. In recent years, Khoury AZ and coworkers carried out systematic theoretical and experimental research on the double or triple OPOs pumped by a continuous wave vortex, and realized the control of the down converted vortex beams [10–12]. Omatsu T and coworkers generated vortex beams from near-IR to mid-IR through the nanosecond pulse vortex pumped OPO, and demonstrated that the distribution of pump OAM in down converted beams are determined by the mode overlap ratio between the pump and the resonant waves in the nonlinear gain [13–17]. Samanta GK et al. reported the operational characteristics of OPO pumped by a picosecond pulse vortex beam [18–22] and the doubly resonant OPO pumped by a cw vortex beam [23]. Hu ML and coworkers realized the tunable vortex signal output from the femtosecond pumped OPO by inserting the q-plate and 1/4 wave plate in the resonant cavity to convert the signal mode from fundamental Gaussian to vortex [27,28]. Zhu XZ et al. studied the backward OPO pumped by vortex beams [29]. Yusufu T presented the SRO pumped by the laser sources with nanosecond (picosecond) pulse duration, and realized the vortex signal (idler) output by adjusting the loss of the resonant wave in the cavity [30–32]. For cw vortex pumped SRO, due to the low parametric gain, the threshold is rather large. The cw SRO is more sensitive to the cavity parameters, and the methods to control the transfer of pump OAM are also limited. In the cw vortex pumped SRO performed by Samanta GK et al., the pump OAM can only be transferred to the non-resonant idler OAM [24–26]. It is still unable to realize the arbitrary transfer of the pump OAM in the SRO under cw operation.

In this paper, a theoretical study of the operation characteristics of the cw SRO under different pump schemes, such as single-pass-pumping (SPP) and double-pass-passing (DPP), are presented. Simple analytic solutions of the coupled-mode equations for the SRO under collimated Gaussian beam approximation are outlined in Section 2. Simulations for experimental results are performed by using the real experimental parameters in Section 3. The resonant signal mode in the SRO is also analyzed for different conditions (mode overlap ratio between the pump and the resonant waves, and defect-size of the spot-defect mirror) in Section 4. Finally, the discussion and conclusion are presented in Sections 5 and 6, respectively. This study provides the guideline for the design of the vortex signal output from the cw vortex pumped SRO with a relatively low oscillation threshold.

2. Theoretical Description of Output Characteristics for Different SROs

In order to give a guideline for the design and optimization of the vortex pumped SRO, the theoretical model for the SRO is presented. Figure 1 shows the schematic of the SROs to be investigated in our theoretical analysis. For the SPP-SRO [as shown in Figure 1a], the coating parameters of the input coupler (M1) and output coupler (M2) are the same. They are high transmission for the pump and idler, and high reflection for the resonant signal. The optical parametric process only occurs in the forward leg. For the DPP-SRO [as shown in Figure 1b], the coating parameter of the input coupler (M1) is high transmission for the

pump and idler, and high reflection for the resonant signal, while the coating parameter of the output coupler (M2) is high transmission for the idler, and high reflection for the pump and resonant signal. The optical parametric process occurs in both the forward leg and the backward leg. Since the loss of intra-cavity signal power in the cavity is small ($V_s < 0.1$), the intra-cavity signal power is assumed to be constant. Using the slowly varying envelope approximation, the coupled-wave equations in the SRO are given by [36–38]

$$dA_p/dz = i4\pi d A_i A_s \exp(-i\Delta k z)/n_p\lambda_p, \tag{1a}$$

$$dA_i/dz = i4\pi d A_i A_s^* \exp(i\Delta k z)/n_i\lambda_i. \tag{1b}$$

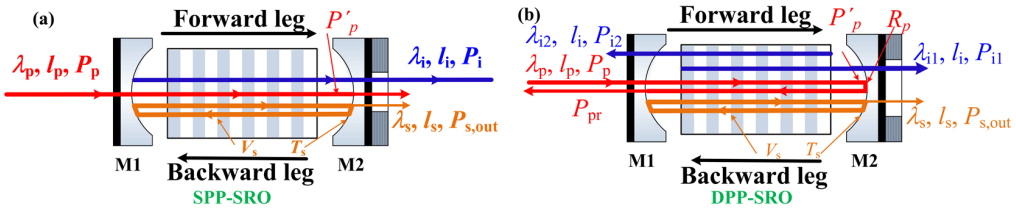

Figure 1. Schematic of the SROs under different pump schemes. (**a**) Single-pass pumping scheme, (**b**) Double-pass pumping scheme.

Here, A_j is the amplitude of the wave j in the SRO crystal. The subscripts p, s, and i denote the pump, signal and idler fields, respectively. d is the effective nonlinear coefficient of the SRO. $\Delta k = 2\pi n_p/\lambda_p - 2\pi n_s/\lambda_s - 2\pi n_i/\lambda_i - 2\pi/\Lambda$ is the phase mismatching condition in the first order quasi-phase matching crystal based-SRO. n_j is the extraordinary refractive index in the quasi-phase matching crystal with a poled period of Λ at the wavelength λ_j. Since the focusing parameters of pump and signal were usually selected to be less than 1 ($\xi_{p,s} \leq 1$, the Rayleigh length is longer than the crystal length) in the real experiments, and the collimated Laguerre-Gaussian (LG) vortex beam approximation is adopted. Meanwhile, the phase mismatch and thermal effects induced by the absorption of nonlinear crystals are ignored for simplicity.

The pump and signal amplitudes in the SRO crystal can be solved as

$$A_p(z) = A_p(0)\cos(qz), \tag{2a}$$

$$A_i(z) = iq_1 A_p(0)\sin(qz)/q. \tag{2b}$$

Here, the parameters q_1, q_2, and q are expressed as

$$q_1 \equiv \frac{4\pi d}{\lambda_i n_i} A_s^*; q_2 \equiv \frac{4\pi d}{\lambda_p n_p} A_s; q \equiv \sqrt{q_1 q_2}. \tag{3}$$

The typical amplitude distribution of the optical field for LG vortex beams LG_{0l} carrying TC l can be expressed as:

$$A_{0l}(r) = \sqrt{\frac{P_{0l}}{\pi n c \varepsilon_0 |l|! w^2}} \left(\frac{\sqrt{2}r}{w^2}\right)^{|l|} \exp(-\frac{r^2}{w^2}) \exp(il\theta). \tag{4}$$

Here, $P_{0l} = 2\pi \int_0^\infty r dr 2nc\varepsilon_0 |A_{0l}(r)|^2$ is the power of the vortex beam, n is the refractive index of the transmission medium, ε_0 is the permittivity of the vacuum, and c is the light speed in vacuum. $w_{0l} = w(|l|+1)^{1/2}$ and w are the beam radii of the LG_{0l} vortex beam and the fundamental mode (LG_{00}) of the LG_{0l} mode, respectively. r, θ and z are the radial, azimuth, and longitudinal coordinates, respectively.

2.1. SPP-SRO

In this case, the optical parametric process only occurs in the forward leg. The signal power gain ΔP_s on the forward leg is given as [36–38]:

$$\begin{aligned}\Delta P_s &= -8d\varepsilon_0\omega_s \mathrm{Im}\int A_s^* A_p A_i^* \mathrm{d}x\mathrm{d}y\mathrm{d}z = 8d\varepsilon_0\omega_s\int_0^\infty \mathrm{d}r 2\pi r \frac{q_1^*}{q} A_s^* \left|A_p(r,0)\right|^2 \int_0^{l_{OPO}} \mathrm{d}z \sin(qz)\cos(qz) \\ &= \frac{2\lambda_p}{\lambda_s}\frac{P_{p0}}{|l_p|!}\int_0^\infty \exp(-2u)(2u)^{|l_p|}\sin^2\left[gl_{OPO}\exp(-\frac{r^2}{w_s^2})\left(\frac{\sqrt{2}r}{w_s}\right)^{|l_s|}\right]\mathrm{d}u = \lambda_p P_{p0}\theta/\lambda_s\end{aligned} \tag{5}$$

Here $P_{p0} = n_p c\varepsilon_0 \pi w_p^2 \left|A_{p0}\right|^2$ is the incident pump power. $\omega_s = 2\pi c/\lambda$ is the angular frequency of the signal light. l_{OPO} is the length of nonlinear crystal. θ represents the proportion of pump power converted in the SRO process of the forward leg,

$$\theta = \frac{2}{|l_p|!}\int_0^\infty \exp(-2u)(2u)^{|l_p|}\sin^2\left[gl_{OPO}\exp(-\frac{r^2}{w_s^2})\left(\frac{\sqrt{2}r}{w_s}\right)^{|l_s|}\right]\mathrm{d}u. \tag{6}$$

g is defined by:

$$g^2 l_{OPO}^2 = \frac{32\pi^2 d^2 l_{OPO}\xi_s P_s}{n_p n_i \lambda_i \lambda_s \lambda_p c\varepsilon_0 |l_s|!}. \tag{7}$$

Here $P_s = n_s c\varepsilon_0 \pi w_s^2 |A_s|^2$ is the intracavity signal power. To simplify the expression above, the mode overlap ratio between pump beam and signal mode (m) and the normalized parameter (u) are introduced:

$$m = w_p^2/w_s^2;\ u = r^2/w_p^2. \tag{8}$$

The focus factor $\xi_{p,s} = l_{OPO}/(k_{p,s}{w_{p,s}}^2)$, and the wave vector $k_{p,s,i} = 2\pi n_{p,s,i}/\lambda_{p,s,i}$.
The oscillation condition for the signal light in SRO is

$$\Delta P_s = P_s(T_s + V_s) = \lambda_p P_p \theta/\lambda_s. \tag{9}$$

Here T_s is the transmission of the output coupler for the signal, and V_s is the roundtrip power loss caused by non-ideal factors, such as scattering and Fresnel loss of the resonator mirrors and crystals surfaces. For each incident pump power P_{p0}, the intracavity signal power P_s can be solved from Equation (9).

Near the threshold, the pump depletion in the SRO crystal can be ignored, and the intracavity signal power is low. The parameter gl_{OPO} is far less than 1 ($gl_{OPO} << 1$), and Equation (6) can be approximated as

$$\theta = \frac{2g^2 l_{OPO}^2}{|l_p|!}\int_0^\infty \exp(-2u)(2u)^{|l_p|}\exp(-\frac{2r^2}{w_s^2})\left(\frac{2r^2}{w_s^2}\right)^{|l_s|}\mathrm{d}u = \frac{g^2 l_{OPO}^2 m^{|l_s|}(|l_p|+|l_s|)!}{|l_p|!(1+m)^{|l_p|+|l_s|+1}}. \tag{10}$$

Substituting Equation (10) into Equation (9), the corresponding threshold pump power of the SPP-SRO can be expressed as

$$P_{th}^{SPP-SRO} = \frac{n_p n_i c\varepsilon_0 \lambda_s^2 \lambda_i (T_s + V_s)|l_p|!|l_s|!(m+1)^{|l_p|+|l_s|+1}}{32\pi^2 d^2 l_{OPO}\xi_s(|l_p| + |l_s|)!m^{|l_s|}}. \tag{11}$$

2.2. DPP-SRO

In this case, the optical parametric process occurs in both the forward leg and the backward leg. The pump power at the end of the nonlinear crystal on the forward leg can be read as:

$$P_p{}' = \left(P_{p0} - \Delta P_s \lambda_s/\lambda_p\right) = P_{p0}(1-\theta). \tag{12}$$

Similarly, the signal power gain $\Delta P'_s$ on the forward leg is given as:

$$\begin{aligned}\Delta P'_s &= 8d\varepsilon_0\omega_s \mathrm{Im}\int A'^{*}_s A'_p A'^{*}_i \mathrm{d}x'\mathrm{d}y'\mathrm{d}z' \\ &= \frac{2\lambda_p}{\lambda_s}\frac{P'_p}{|l_p|!}\int_0^{\infty}\exp(-2u')(2u')^{|l_p|}\sin^2\left[g' l_{OPO}\exp(-\frac{r'^2}{w'^2_s})\left(\frac{\sqrt{2}r'}{w_s}\right)^{|l_s|}\right]\mathrm{d}u' = \lambda_p P'_p\theta'/\lambda_s\end{aligned} \quad (13)$$

where z' is the new coordinate axis along the backward direction, and $z' = 0$ indicates the end of the crystal on the forward leg. $A'_{p,s,i}$ represent the amplitudes of the pump, signal and idler fields on the backward leg, respectively. θ' represents the proportion of pump power converted in the SRO process of the backward leg,

$$\theta' = \frac{2}{l_p!}\int_0^{\infty}\exp(-2u')(2u')^{l_p}\sin^2\left[g' l_{OPO}\exp(-\frac{r'^2}{w'^2_s})\left(\frac{\sqrt{2}r'}{w'_s}\right)^{l_s}\right]\mathrm{d}u' = \theta. \quad (14)$$

g' is defined by:

$$g'^2 l^2_{OPO} = \frac{32\pi^2 d^2 l_{OPO}\xi_s P_s}{n_p n_i \lambda_i \lambda_s \lambda_p c\varepsilon_0 |l_s|!} = g^2 l^2_{OPO}. \quad (15)$$

When the DPP-SRO is operated stably, the oscillation condition is:

$$\Delta P_s + \Delta P_s{}' = P_s(T_s + V_s) = \lambda_p P_{p0}[(1-\theta)\theta + \theta]/\lambda_s = \lambda_p P_{p0}(2-\theta)\theta/\lambda_s. \quad (16)$$

P_s can be obtained as an implicit function of the incident pump power P_{p0}. The threshold pump power of the DPP-SRO is given by

$$P^{DPP-SRO}_{th} = \frac{n_p n_i c\varepsilon_0 \lambda_s^2 \lambda_i (T_s + V_s)|l_p|!|l_s|!(m+1)^{|l_p|+|l_s|+1}}{64\pi^2 d^2 l_{OPO}\xi_s(|l_p| + |l_s|)!m^{|l_s|}}. \quad (17)$$

If a spot-defect mirror [39,40] is used as the output coupler, the transmission T'_s of the spot-defect mirror on the resonant transverse mode can be calculated as:

$$T'_s = \frac{1}{|l_s|!}\int_0^{r_a}\left(\frac{2r^2}{W_s^2}\right)^{|l_s|}\exp(-\frac{2r^2}{W_s^2})r\mathrm{d}r = \frac{1}{|l_s|!}\int_0^{\nu_a}\nu^{|l_s|}\exp(-\nu)\mathrm{d}\nu \quad (18)$$

Here $\nu = 2r^2/W_s^2$. $W_s(|l|+1)^{1/2}$ is the radius of resonant signal mode LG_{0l} on the spot-defect mirror, and r_a is the radius of spot-defect on the output coupler. At this time, the output coupler T_s shown above should be replaced by $(T_s + T'_s)$.

The extracted signal power from the SRO is given by

$$P_{s,out} = (T_s + T'_s)P_s. \quad (19)$$

The signal extraction efficiency and pump depletion can be written as:

$$\eta_{p-s} = \frac{P_{s,out}}{P_{p0}} = \frac{P_s(T_s + T'_s)}{P_{p0}}, \quad (20)$$

$$\eta_{dep} = \frac{\lambda_s(T_s + T'_s + V_s)P_s}{\lambda_p P_{p0}}. \quad (21)$$

3. Output Characteristics of Vortex Pumped SROs

Output characteristics of different SROs are numerically calculated using the theory shown in Section 2. Without special statements, the parameters used in our numerical calculations are: $\varepsilon_0 = 8.854 \times 10^{-12}$ As/(Vm), $c = 3.0 \times 10^8$ m/s, d =16 pm/V, l_{OPO} = 50 mm, λ_p = 1.064 μm, λ_s = 1.538 μm, λ_i = 3.452 μm, n_p = 2.16, n_s = 2.15, n_i = 2.09, $T_s + V_s$ = 5.0%, ξ_s = 1, and m = 0.686, respectively.

The pump depletions of DPP-SRO and SPP-SRO as functions of pump ratio (the ratio between the pump power and the threshold) under different m values for different combinations of pump vortex order l_p and resonant signal vortex order l_s (l_p = 1, l_s = 0 and l_p = 2, l_s = 0) are shown in Figure 2. According to the threshold expressions shown in Equations (11) and (17), the threshold of the DPP-SRO is half that of the SPP-SRO. To compare these two cases, Figure 2 is plotted using the pump ratio of DPP-SRO as the horizontal ordinate. It can be seen that the pump depletions decrease with increasing m under the same pump ratio, and the DPP-SRO can realize higher pump depletion over a wider pumping range than the SPP-SRO at the same m. The maximum pump depletion happens at the pump ratio of about 3–5 for DPP-SRO and 2–3 for SPP-SRO, respectively.

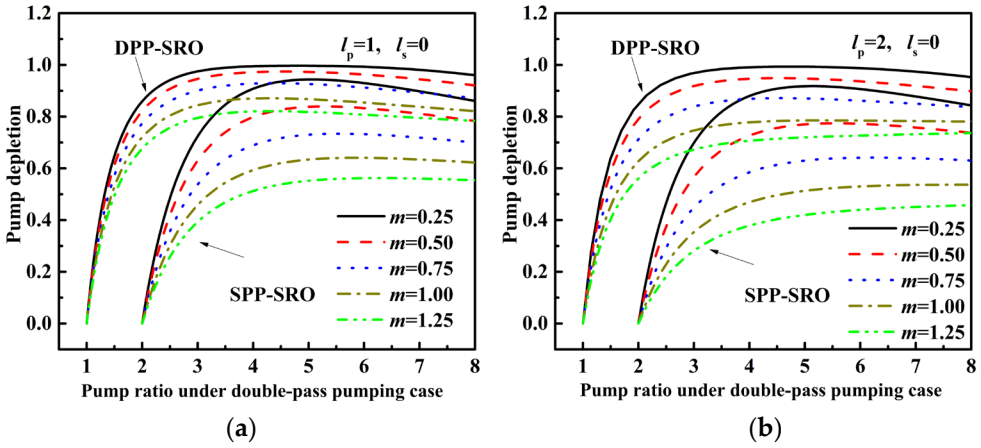

Figure 2. Pump depletion of SROs versus pump ratio under different m. l_s = 0 and l_p = 1 (**a**); and l_p =2 (**b**).

Numerical simulations of experiment output characteristics of vortex pumped SRO performed by A. Aadhi et al. [24] are shown in Figure 3. The simulation parameters are chosen according to the experimental conditions and the beam waists w of pump and signal are chosen such that the theoretical calculations fit the experimental results well, since the thermal lens effects of nonlinear crystal due to the absorption of interaction waves will change the beam waists in nonlinear crystal. The specific fitting parameters are: λ_p = 1.064 μm, λ_s = 1.972 μm, λ_i = 2.310 μm, n_p = 2.20, n_s = 2.17, n_i = 2.16, $T_s + V_s$ = 6.3%, w_p = 85 μm (for l_p = 1) or 81 μm (for l_p = 2), and w_s = 91 μm (for l_p = 1) or 75 μm (for l_p = 2). The good agreement between the theoretical analysis and the experimental results verified once again the correctness of our theory.

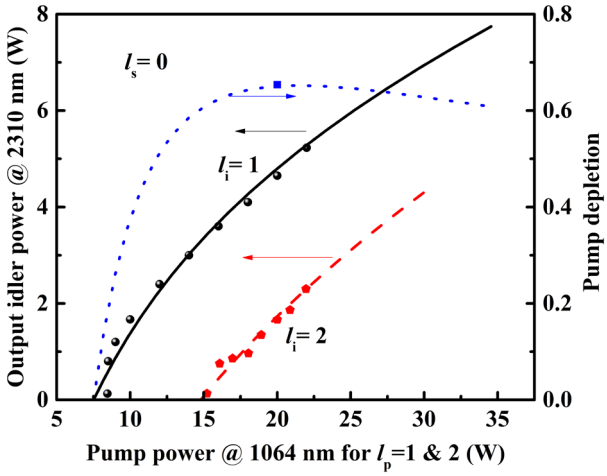

Figure 3. Numerical simulations of output characteristics for SPP-SRO performed by A. Aadhi et al. [24]. Lines are numerical simulations and dots are experimental results.

4. Predictions for the Resonant Signal Mode in SROs

For vortex pumped SROs, the oscillation threshold determines how the OAM of the pump beam is transferred to two down converted beams. The SRO tends to oscillate with the resonant signal mode that has the lowest oscillation threshold. The oscillation threshold of SPP-SRO for different pump vortex order l_p, mode overlap ratio between the pump and the signal m, and the defect size of spot-defect mirror r_a, are numerically calculated.

Figure 4 shows the calculated threshold of the SPP-SRO for different vortex orders of the pump and the resonant signal using the formula shown in Equation (11). With the increase of pump vortex order l_p, the resonant signal mode with higher vortex order l_s has the lower oscillation threshold. It shows that the SRO tends to oscillate with higher signal vortex order l_s for higher pump vortex order l_p. In addition, we also find that the oscillation threshold increases with increasing the vortex order of pump l_p.

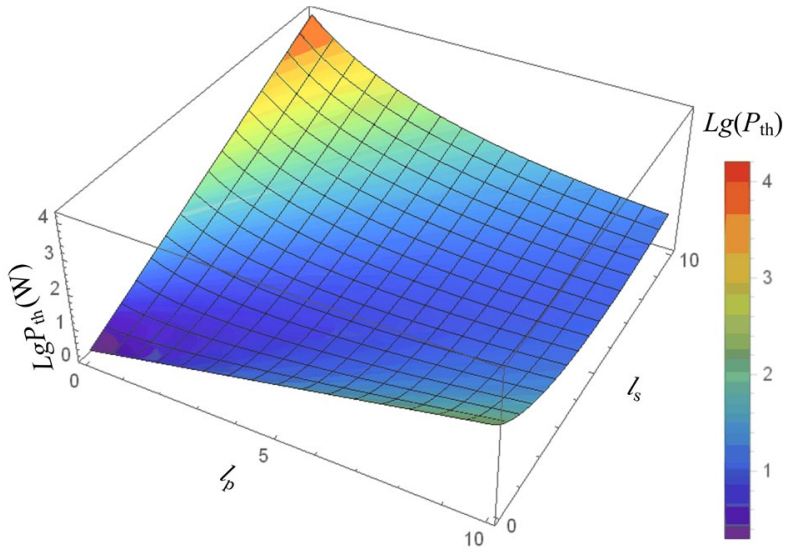

Figure 4. Threshold of the SPP-SRO for different combinations of pump vortex order l_p and resonant signal vortex order l_s in logarithmic coordinate.

Figure 5 shows the oscillation threshold versus the mode overlap ratio m for different combinations of pump and signal vortex orders. For $l_p = 0$ (fundamental Gaussian beam) shown in Figure 5a, the resonant signal mode l_s in SRO keeps the fundamental Gaussian beam ($l_s = 0$) for m changing from 0.2 to 2, and other signal modes ($l_s \neq 0$) are far from oscillation; considering that the vortex order of the signal light is no bigger than that of the pump, we only calculate the oscillation threshold for the case $l_s \leq l_p$ below. For $l_p = 1$, shown in Figure 5b, the resonant signal mode l_s in SRO oscillates with the fundamental Gaussian beam ($l_s = 0$) for $0.2 < m < 1$, vortex mode with $l_s = 1$ for $1 < m < 2$; For $l_p = 2$ shown in Figure 5c, the resonant signal mode l_s in SRO oscillates with the fundamental Gaussian beam ($l_s = 0$) for $0.2 < m < 0.5$, vortex mode with $l_s = 1$ for $0.5 < m < 1$, and vortex mode with $l_s = 2$ for $1 < m < 2$, respectively; For $l_p = 3$ shown in Figure 5d, the resonant signal mode l_s in SRO oscillates with the fundamental Gaussian beam ($l_s = 0$) for $0.2 < m < 1/3$, vortex mode with $l_s = 1$ for $1/3 < m < 2/3$, vortex mode with $l_s = 2$ for $2/3 < m < 1$, and vortex mode with $l_s = 3$ for $1 < m < 2$, respectively. These results show that the signal light in SRO tends to oscillate with the fundamental Gaussian mode for small m (small pump beam spot), and leaves the OAM of pump light transferring to the OAM of the idler beam. The conclusion is consistent with the early experimental results [24]. By carefully controlling the pump beam size w_p in nonlinear crystal, different OAM transfer requirements of pump light in SRO can be achieved. However, as the pump mode overlap ratio m (pump beam size w_p) becomes larger, the oscillation threshold also increases.

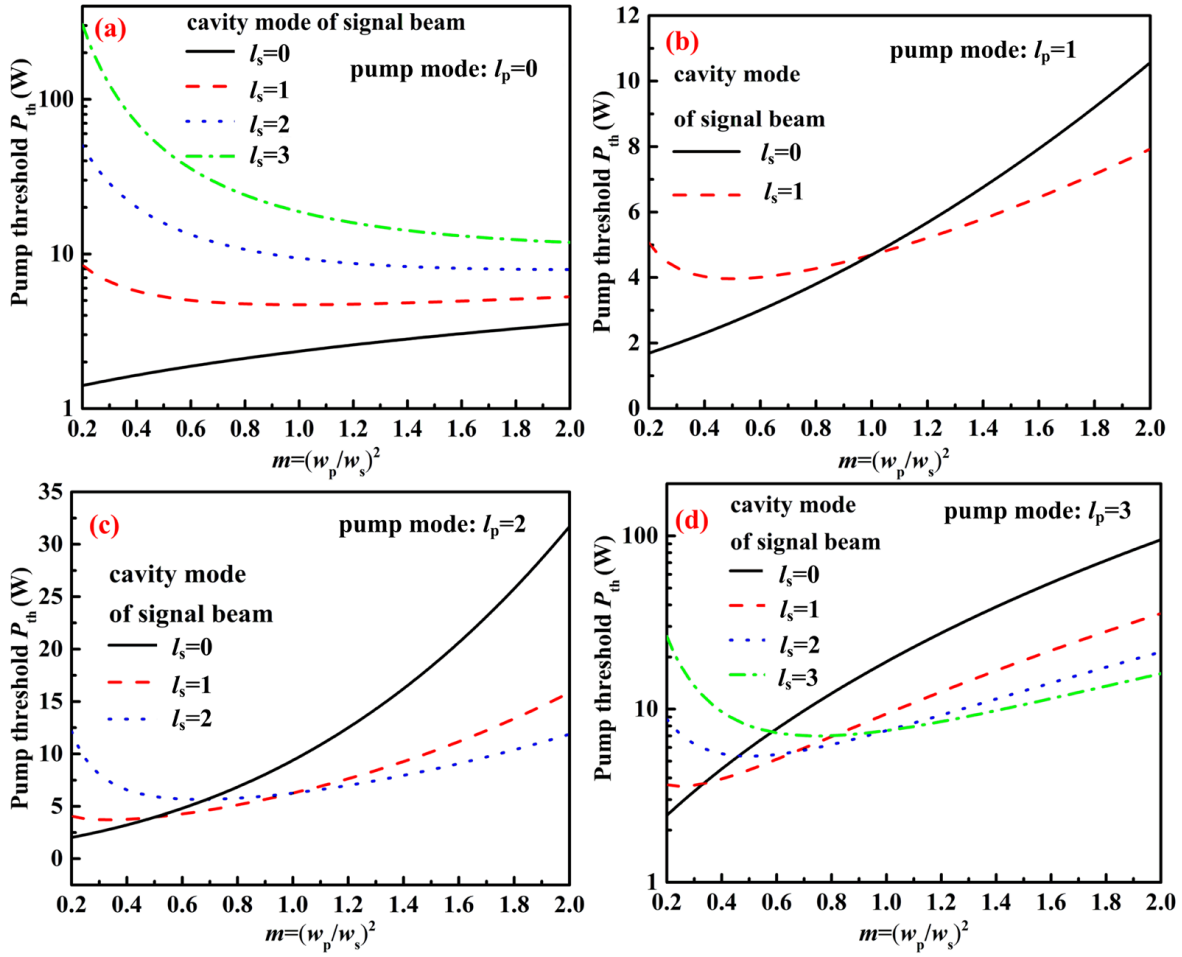

Figure 5. Theoretical predictions for the threshold of SPP-SRO versus the mode overlap ratio m for different combinations of pump vortex order l_p and resonant signal vortex order l_s. (**a**). l_p = 0; (**b**). l_p = 1; (**c**). l_p = 2; (**d**). l_p = 3. w_s = 76 μm.

The relationships between the threshold of SPP-SRO versus the defect radius r_a for different combinations of pump and signal vortex orders are presented in Figure 6. The threshold increases slowly (almost unchanged) with the increase of r_a for $l_s \neq 0$, and the larger the value of l_s, the wider the range of r_a that keeps the threshold nearly unchanged. As shown in Figure 6a, the signal wave with l_s = 1 can oscillate at the threshold of 5 W in the fundamental Gaussian beam pumped SPP-SRO for r_a = 36.5 μm (0.21 W_s). For l_p = 1 shown in Figure 6b, the signal wave with l_s = 1 can oscillate at the threshold of about 4.2 W in the SPP-SRO for r_a changing from 14 μm (0.08 W_s) to 40 μm (0.23 W_s). For l_p = 2 shown in Figure 6c, the signal wave with l_s = 1 can oscillate at the threshold less than 5 W in the SPP-SRO for r_a less than 40 μm (0.23 W_s), and the signal wave with l_s = 2 can oscillate at the threshold less than 6 W in the SPP-SRO for 50 μm (0.29 W_s) < r_a < 70 μm (0.40 W_s). For l_p = 3 shown in Figure 6d, the signal wave with l_s = 2 can oscillate at the threshold less than 6 W in the SPP-SRO for r_a < 70 μm (0.40 W_s), and the signal wave with l_s = 3 can oscillate at the threshold less than 8 W in the SPP-SRO for r_a changing from 90 μm (0.52 W_s) to 100 μm (0.57 W_s). It can be seen that the spot-defect cavity mirror makes SRO oscillating with the high-order signal mode under high-order LG0l mode pumping. It can be seen that the spot-defect cavity mirror makes SRO oscillating with the high-order signal mode under high-order LG_{0l} mode pumping. Thus, by selecting the appropriate size of the spot-defect on the output coupler, the high-order signal mode can oscillate in SRO without significantly increasing the threshold.

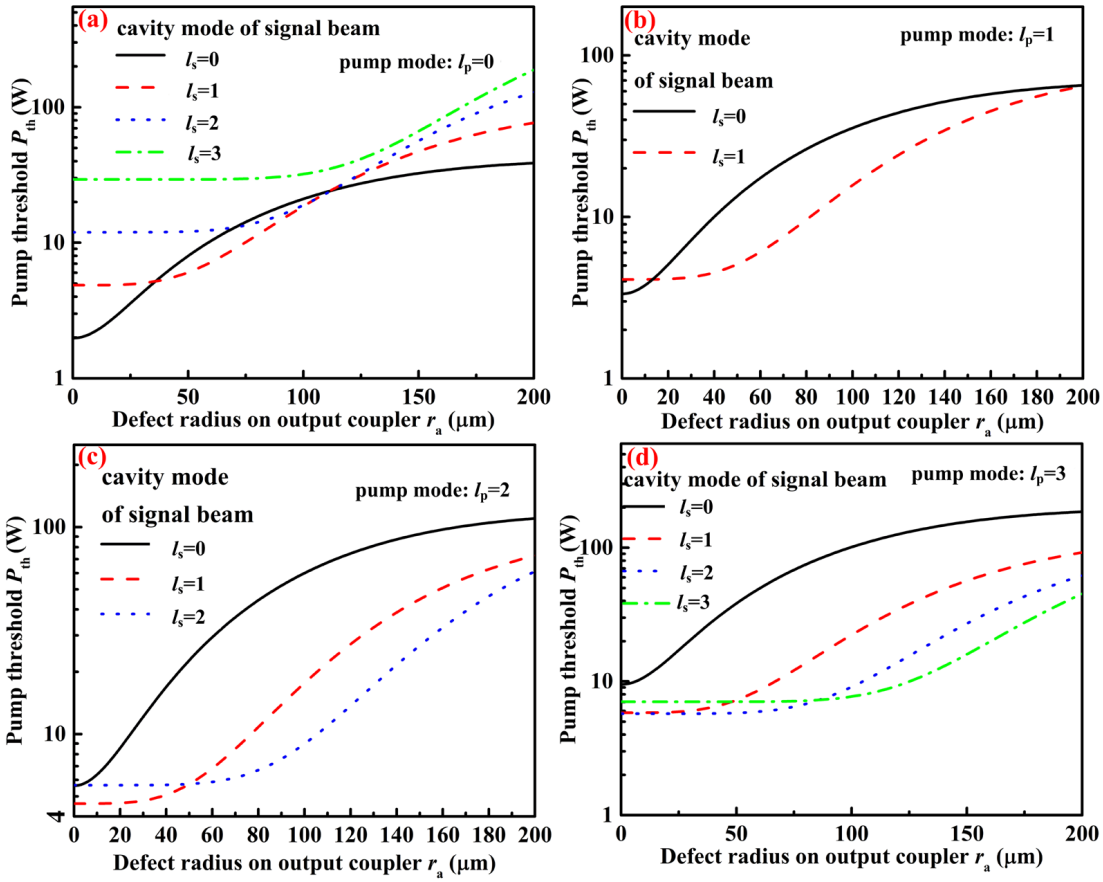

Figure 6. Theoretical predictions for the threshold of SPP-SRO versus the defect radius on output coupler r_a for different combinations of pump vortex order l_p and resonant signal vortex order l_s. Here w_p = 63 μm, m = 0.686. The beam radius of the signal wave on the output coupler is W_s = 174 μm. (**a**). l_p = 0; (**b**). l_p = 1; (**c**). l_p = 2; (**d**). l_p = 3.

5. Discussion

Two transverse mode control methods, including the gain-control method and the loss-control method, can be employed to oscillate at a high order signal mode in SRO. For the gain-control method, the pump vortex order l_p and mode overlap ratio m between the pump and signal in nonlinear crystal can be used in an experiment. The SRO will oscillate with a higher order signal vortex for a higher order pump vortex. By carefully controlling the pump beam spot w_p (mode overlap ratio m) in nonlinear crystal, a signal mode with different vortex orders will oscillate in SRO. For the loss-control method, the spot-defect mirror will be used as one cavity mirror of the SRO cavity, and it will introduce different degrees of loss for a different order signal vortex. The SRO can oscillate with high order signal mode at a relatively low pump threshold by employing the spot-defect mirror with proper spot-defect size.

6. Conclusions

In summary, the model describing the vortex pumped SRO under collimated Gaussian beam approximation is set up. The SRO threshold for the double-passing case is half that for single-pass pumping case, and the DPP-SRO can keep high efficiency over a wide pumping range. The oscillation threshold for different combinations of pump vortex order l_p and resonant signal vortex order l_s, different mode overlap ratio m between the pump and signal in nonlinear crystal, and the spot-defect radius on output coupler r_a is numerically calculated. Our study provides a new design idea for the vortex pumped SRO under cw operation to arbitrarily transfer the OAM of a pump to that of the down converted beams.

Author Contributions: Conceptualization, Z.Z. and P.L.; investigation, Z.Z, S.Z., Y.D., M.G. and P.L.; data curation, Z.Z., M.G. and P.L.; writing—original draft preparation, Z.Z. and P.L.; theoretical calculation, Z.Z., S.Z. and P.L.; writing—review and editing, S.Z. and P.L.; funding acquisition, P.L. All authors have read and agreed to the published version of the manuscript.

Funding: This work was supported by the Scientific and Technological Developing Scheme of Henan Province (202300410072), Key Scientific Research Project of Colleges and Universities in Henan Province (18A140002), the National Natural Science Foundation of China (NSFC) (12104131).

Institutional Review Board Statement: Not applicable.

Informed Consent Statement: Not applicable.

Conflicts of Interest: The authors declare that they have no conflicts of interest.

References

1. Shen, Y.; Wang, X.; Xie, Z.; Min, C.; Fu, X.; Liu, Q.; Gong, M.; Yuan, X. Optical vortices 30 years on: OAM manipulation from topological charge to multiple singularities. *Light Sci. Appl.* **2021**, *8*, 90. [CrossRef] [PubMed]
2. Mun, J.; Kim, M.; Yang, Y.; Badloe, T.; Ni, J.; Chen, Y.; Qiu, C.-W.; Rho, J. Electromagnetic chirality: From fundamentals to nontraditional chiroptical phenomena. *Light Sci. Appl.* **2020**, *9*, 139. [CrossRef] [PubMed]
3. Reddy, I.V.; Baev, A.; Furlani, E.P.; Prasad, P.N.; Haus, J.W. Interaction of Structured Light with a Chiral Plasmonic Metasurface: Giant Enhancement of Chiro-Optic Response. *ACS Photon.* **2018**, *5*, 734–740. [CrossRef]
4. Wu, T.; Wang, R.-Y.; Zhang, X. Plasmon-induced strong interaction between chiral molecules and orbital angular momentum of light. *Sci. Rep.* **2015**, *5*, 18003. [CrossRef]
5. Ni, J.; Liu, S.; Wu, D.; Lao, Z.; Wang, Z.; Huang, K.; Ji, S.; Li, J.; Huang, Z.; Xiong, Q.; et al. Gigantic vortical differential scattering as a monochromatic probe for multiscale chiral structures. *Proc. Natl. Acad. Sci. USA* **2021**, *118*, e2020055118. [CrossRef]
6. Ni, J.; Liu, S.; Hu, G.; Hu, Y.; Lao, Z.; Li, J.; Zhang, Q.; Wu, D.; Dong, S.; Chu, J.; et al. Giant Helical Dichroism of Single Chiral Nanostructures with Photonic Orbital Angular Momentum. *ACS Nano* **2021**, *15*, 2893–2900. [CrossRef]
7. Brullot, W.; Vanbel, M.K.; Swusten, T.; Verbiest, T. Resolving enantiomers using the optical angular momentum of twisted light. *Sci. Adv.* **2016**, *2*, e1501349. [CrossRef]
8. Xiao, N.; Fan, J.; Zhao, J.; Yang, W.; Xie, C.; Hu, M. Intrinsic conservation nature of orbital angular momentum in a vortex-pumped femtosecond optical parametric amplifier. *J. Phys. D Appl. Phys.* **2020**, *53*, 115104. [CrossRef]
9. Arlt, J.; Dholakia, K.; Allen, L.; Padgett, M.J. Efficiency of second-harmonic generation with Bessel beams. *Phys. Rev. A* **1999**, *59*, 3950–3952. [CrossRef]
10. Martinelli, M.; Huguenin, J.A.O.; Nussenzveig, P.; Khoury, A.Z. Orbital angular momentum exchange in an optical parametric oscillator. *Phys. Rev. A* **2004**, *70*, 013812. [CrossRef]
11. Alves, G.B.; Barros, R.F.; Tasca, D.S.; Souza, C.E.R.; Khoury, A.Z. Conditions for optical parametric oscillation with a structured light pump. *Phys. Rev. A* **2018**, *98*, 063825. [CrossRef]
12. Barros, R.F.P.D.R.; Alves, G.B.; Tasca, D.; Souza, C.E.R.; Khoury, A.Z. Fine-tuning of orbital angular momentum in an optical parametric oscillator. *J. Phys. B At. Mol. Opt. Phys.* **2019**, *52*, 244002. [CrossRef]
13. Yusufu, T.; Tokizane, Y.; Miyamoto, K.; Omatsu, T. Handedness control in a 2-μm optical vortex parametric oscillator. *Opt. Express* **2013**, *21*, 23604–23610. [CrossRef] [PubMed]
14. Furuki, K.; Horikawa, M.-T.; Ogawa, A.; Miyamoto, K.; Omatsu, T. Tunable mid-infrared (63–12 μm)optical vortex pulse generation. *Opt. Express* **2014**, *22*, 26351–26357. [CrossRef] [PubMed]
15. Abulikemu, A.; Yusufu, T.; Mamuti, R.; Araki, S.; Miyamoto, K.; Omatsu, T. Octave-band tunable optical vortex parametric oscillator. *Opt. Express* **2016**, *24*, 15204–15211. [CrossRef]
16. Mamuti, R.; Araki, S.; Nishida, S.; Miyamoto, K.; Omatsu, T. Tunable near-infrared optical vortex parametric laser with versatile orbital angular momentum states. *Appl. Opt.* **2018**, *57*, 10004–10008. [CrossRef] [PubMed]
17. Mamuti, R.; Goto, S.; Miyamoto, K.; Omatsu, T. Generation of coupled orbital angular momentum modes from an optical vortex parametric laser source. *Opt. Express* **2019**, *27*, 37025–37033. [CrossRef] [PubMed]
18. Aadhi, A.; Samanta, G.K. High-power, high repetition rate, tunable, ultrafast vortex beam in the near-infrared. *J. Opt.* **2018**, *20*, 01LT01. [CrossRef]
19. Sharma, V.; Kumar, S.C.; Samanta, G.K.; Ebrahim-Zadeh, M. Tunable, high-power, high-order optical vortex beam generation in the mid-infrared. *Opt. Express* **2022**, *30*, 1195–1204. [CrossRef]
20. Sharma, V.; Suddapalli, C.K.; Samanta, G.K.; Ebrahim-Zadeh, M. Multi-structured-beam optical parametric oscillator. *Opt. Express* **2020**, *28*, 21650–21658. [CrossRef]
21. Sharma, V.; Kumar, S.C.; Aadhi, A.; Ye, H.; Samanta, G.K.; Ebrahim-Zadeh, M. Tunable vector-vortex beam optical parametric oscillator. *Sci. Rep.* **2019**, *9*, 9578. [CrossRef] [PubMed]
22. Sharma, V.; Kumar, S.C.; Samanta, G.K.; Ebrahim-Zadeh, M. Orbital angular momentum exchange in a picosecond optical parametric oscillator. *Opt. Lett.* **2018**, *43*, 3606–3609. [CrossRef] [PubMed]

23. Aadhi, A.; Samanta, G.K.; Kumar, S.C.; Ebrahim-Zadeh, M. Controlled switching of orbital angular momentum in an optical parametric oscillator. *Optica* **2017**, *4*, 349–355. [CrossRef]
24. Aadhi, A.; Sharma, V.; Singh, R.P.; Samanta, G.K. Continuous-wave, singly resonant parametric oscillator-based mid-infrared optical vortex source. *Opt. Lett.* **2017**, *42*, 3674–3677. [CrossRef]
25. Aadhi, A.; Sharma, V.; Samanta, G.K. High-power, continuous-wave, tunable mid-IR, higher-order vortex beam optical parametric oscillator. *Opt. Lett.* **2018**, *43*, 2312–2315. [CrossRef] [PubMed]
26. Sharma, V.; Samanta, G.K.; Kumar, S.C.; Singh, R.P.; Ebrahim-Zadeh, M. Tunable ultraviolet vortex source based on a continuous-wave optical parametric oscillator. *Opt. Lett.* **2019**, *44*, 4694–4697. [CrossRef]
27. Fan, J.; Zhao, J.; Shi, L.; Xiao, N.; Hu, M. Two-channel, dual-beam-mode, wavelength-tunable femtosecond optical parametric oscillator. *Adv. Photon.* **2020**, *2*, 045001. [CrossRef]
28. Zhao, J.; Fan, J.; Tian, H.; Hu, M.-L. Dual-mode and two-signal-wavelength femtosecond optical parametric oscillator based on LiB_3O_5. *Opt. Lett.* **2020**, *45*, 3985–3988. [CrossRef]
29. Zhu, X.; He, J.; Su, Y.; Chen, Y.; Hu, X. Theoretical Investigation of Backward Optical Parametric Oscillator Pumped by Vortex Beams. *Front. Phys.* **2022**, *10*, 886962. [CrossRef]
30. Niu, S.; Wang, S.; Ababaike, M.; Yusufu, T.; Miyamoto, K.; Omatsu, T. Tunable near- and mid-infrared (1.36–1.63 μm and 3.07–4.81 μm) optical vortex laser source. *Laser Phys. Lett.* **2020**, *17*, 045402. [CrossRef]
31. Ababaike, M.; Wang, S.; Aierken, P.; Omatsu, T.; Yusufu, T. Near and mid-infrared optical vortex parametric oscillator based on KTA. *Sci. Rep.* **2021**, *11*, 8013. [CrossRef] [PubMed]
32. Jashaner, D.; Zhou, Y.; Yusufu, T. Widely-tunable mid-infrared (2.6–5 μm) picosecond vortex laser. *Appl. Phys. Express* **2022**, *15*, 102004. [CrossRef]
33. Navarrete-Benlloch, C.; de Valcárcel, G.J.; Roldán, E. Generating highly squeezed hybrid Laguerre-Gauss modes in large-Fresnel-number degenerate optical parametric oscillators. *Phys. Rev. A* **2009**, *79*, 043820. [CrossRef]
34. Chen, Y.; Liu, S.; Lou, Y.; Jing, J. Orbital Angular Momentum Multiplexed Quantum Dense Coding. *Phys. Rev. Lett.* **2021**, *127*, 093601. [CrossRef] [PubMed]
35. Guo, Y.; Zhang, H.; Guo, X.; Zhang, Y.; Zhang, T. High-order continuous-variable coherence of phase-dependent squeezed state. *Opt. Express* **2022**, *30*, 8461–8473. [CrossRef]
36. Gao, X.; Li, P.; Wu, Z.; Dai, S.; Gu, Y. Theoretical analysis of a continuous-wave 323 nm laser generated by a singly resonant optical parametric oscillator with intracavity sum-frequency generation. *Laser Phys.* **2018**, *28*, 085401. [CrossRef]
37. Li, P.; Li, Y.; Feng, J.; Zhang, K. Theoretical and experimental investigation of singly resonant optical parametric oscillator under double-pass pumping. *Appl. Opt.* **2015**, *54*, 4374–4379. [CrossRef]
38. Li, P.; Ma, J.; Wu, Z.; Xing, T.; Guo, H.; Gu, Y. Optimization of sum frequency output from intra-cavity sum frequency generation in singly resonant optical parametric oscillator. *Laser Phys.* **2020**, *30*, 045403. [CrossRef]
39. Ito, A.; Kozawa, Y.; Sato, S. Generation of hollow scalar and vector beams using a spot-defect mirror. *J. Opt. Soc. Am. A* **2010**, *27*, 2072–2077. [CrossRef]
40. Vyas, S.; Kozawa, Y.; Sato, S. Generation of a vector doughnut beam from an internal mirror He-Ne laser. *Opt. Lett.* **2014**, *39*, 2080–2083. [CrossRef]